

# ppb-Level SO<sub>2</sub> Photoacoustic Sensors with a Suppressed Absorption–Desorption Effect by Using a 7.41 μm External-Cavity Quantum Cascade Laser

Xukun Yin, Hongpeng Wu, Lei Dong,\* Biao Li, Weiguang Ma, Lei Zhang, Wangbao Yin, Liantuan Xiao, Suotang Jia, and Frank K. Tittel



Cite This: *ACS Sens.* 2020, 5, 549–556



Read Online

ACCESS |



Metrics & More



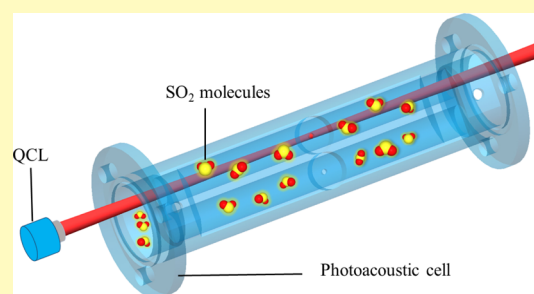
Article Recommendations



Supporting Information

**ABSTRACT:** A sensitive photoacoustic sensor system for the detection of ppb-level sulfur dioxide (SO<sub>2</sub>) was developed by the use of a continuous-wave room-temperature, high-power quantum cascade laser (QCL) with an external diffraction grating cavity geometry. The excitation wavelength of the QCL was set to 7.41 μm for the strongest SO<sub>2</sub> absorption line strength. A custom-made differential photoacoustic cell (PAC) with two identical resonators was designed to allow a gas flow rate up to 1200 sccm. A qualitative theoretical model was employed in order to understand the dynamic adsorption and desorption processes of SO<sub>2</sub> in the PAC walls. A 1σ detection limit of 2.45 ppb, corresponding to a normalized noise equivalent absorption value of  $3.32 \times 10^{-9} \text{ W/Hz}^{1/2}$ , was achieved after measures for suppressing the absorption–desorption effect were taken.

**KEYWORDS:** photoacoustic spectroscopy, trace gas sensor, adsorption–desorption effects, quantum cascade lasers, differential photoacoustic cell, sulfur dioxide detection



Sulfur dioxide (SO<sub>2</sub>) is an invisible and transparent air pollutant with a nasty and pungent odor, which reacts easily with other substances to form harmful compounds, such as sulfate particles, sulfuric, and sulfurous acid. About 99% of ambient SO<sub>2</sub> sources originate from anthropogenic activities such as the burning of fossil fuels, industrial manufacturing, and motor vehicle emissions.<sup>1</sup> According to the United States National Ambient Air Quality Standards (NAAQS), the acceptable safety SO<sub>2</sub> standard is 0.5 ppm for 3 h of exposure in atmospheric air.<sup>2</sup> Trace amounts of SO<sub>2</sub> can cause health and environmental effects. For example, SO<sub>2</sub> can irritate the nose, throat, and respiratory tract to cause symptoms such as coughing, breathlessness, asthma, or a tight feeling around the chest upon inhalation. It was further demonstrated that when an asthma patient inhaled SO<sub>2</sub> concentrations as low as 200–300 ppb for 5–10 min would result in moderate and even greater lung function reduction. Furthermore, SO<sub>2</sub> and sulfur oxides (SO<sub>x</sub>) can react with other atmospheric compounds to form fine particles, which may penetrate deeply into the lungs and cause serious health problems when these particles are accumulated to a certain quantity. In terms of environmental pollution, the deposition of these sulfate particles contributes to particulate matter, haze and acid rain pollution, which can stain and damage stone, bronze, and other materials, including culturally important heritages such as statues, sculptures, and monuments.<sup>3–6</sup> Therefore, there is a requirement to develop a reliable, cost-effective, highly sensitive, and selective SO<sub>2</sub> trace

gas sensor for human health protection and ecological air quality monitoring.

Up to now, various trace SO<sub>2</sub> gas sensors based on different detection techniques have been reported, such as amperometric sensors,<sup>7</sup> carbon nanotubes,<sup>8</sup> mass spectrometry,<sup>9</sup> chemiluminescence,<sup>10,11</sup> and electrochemical sensors.<sup>12</sup> However, most of these chemical-based sensors have a long response time, a short service life, a low detection sensitivity, and selectivity. For example, the fluorescence analysis is a commonly used method to detect SO<sub>2</sub>, in which the fluorescent aldehyde or levulinate-based probes were used to specifically react with SO<sub>2</sub> or its derivatives. Therefore, the detection sensitivity may suffer from interference from sulfur-containing molecules and induce a high background signal. Moreover, there are some unavoidable active gas molecules such as H<sub>2</sub>S, NO, NO<sub>2</sub> and NH<sub>3</sub> in air during the detection of SO<sub>2</sub>, which may react with the sensor materials and thus influence the SO<sub>2</sub> detection limit. Therefore, it is a big challenge to detect trace levels of SO<sub>2</sub> by using these chemical-based sensors.

**Received:** December 10, 2019

**Accepted:** January 15, 2020

**Published:** January 15, 2020

Because different gas chemical species have their unique absorption lines, the laser-based photoacoustic spectroscopy (PAS) detection technology was developed rapidly, which offers a large gas specificity capable of higher detection selectivity as well as real-time in situ measurements. One of the distinct features of the PAS technology is that photoacoustic sensors detect the light-induced sound wave and hence do not depend on the excitation optical wavelength. As a result, numerous PAS-based sensors were developed by employing different excitation sources in electronic (UV–Vis),<sup>13,14</sup> vibrational overtone (1–2.5  $\mu\text{m}$ ),<sup>15–17</sup> fundamental transitions (3–12  $\mu\text{m}$ ),<sup>18–23</sup> and in the rotational (THz range) spectral region.<sup>24–26</sup> Somesfalean et al. in 2005 used an UV spectrometer with a 6.9 nW diode laser emitting at 302 nm, achieving a detection limit of 20 ppmv at atmospheric pressure.<sup>27</sup> However, there are some other molecules with absorption bands at around 302 nm ( $\text{O}_3$ ,  $\text{H}_2\text{CO}$ ,  $\text{NO}_2$ ). The laser power fluctuations associated with the sum-frequency UV laser generation limit the sensor sensitivity in the practical applications.<sup>28,29</sup> Therefore, it is optimal for PAS-based sensors to detect  $\text{SO}_2$  in the fundamental transition region because of the strong absorption features and the high output power from commercially available quantum cascade lasers (QCLs) or interband cascade lasers (ICLs). In 2014, Waclawek et al.<sup>30</sup> developed a quartz-enhanced PAS (QEPAS)-based sensor system for  $\text{SO}_2$  detection by using a mid-infrared distributed feedback quantum cascade (DFB-QCL) operating at 7.24  $\mu\text{m}$ , and a minimum detection limit of 63 ppbv was achieved. Several  $\text{SO}_3$  and  $\text{H}_2\text{O}$  absorption lines exist around the 7.24  $\mu\text{m}$  and can cause detection interference. Furthermore, a degraded beam from the DFB-QCL laser resulted in a  $\sim 8.2$  times higher background noise compared to the calculated thermal noise because the narrow gap between the quartz tuning fork prongs is 300  $\mu\text{m}$ .<sup>31</sup>

In this manuscript, a continuous-wave (CW) external cavity QCL emitting at 7.41  $\mu\text{m}$  combining with a custom-made differential photoacoustic cell (PAC) was employed for the first time, to the best of our knowledge, to detect trace  $\text{SO}_2$  in the mid-IR. The large inner diameter of the two resonators and the differential PAC configuration could reduce the background noise, response time, and thus obtain an optimal detection limit at the ppb level. The dynamic adsorption–desorption interaction processes of  $\text{SO}_2$  with the PAC walls were also investigated by means of a qualitative theoretical model and experiments because the adsorption or desorption effects result in a change of the gas-phase concentration.

## SELECTION OF OPTICAL EXCITATION SOURCE

HITRAN database provides six spectral absorption regions of the  $\text{SO}_2$  molecule, that is, 2.5  $\mu\text{m}$  ( $3\nu_3$ ), 3.7  $\mu\text{m}$  ( $2\nu_3$ ), 4.0  $\mu\text{m}$  ( $\nu_1 + \nu_3$  and  $\nu_1 + \nu_2 + \nu_3 - \nu_2$ ), 7.3  $\mu\text{m}$  ( $\nu_3$ ), 8.6  $\mu\text{m}$  ( $\nu_1$ ), and 19.3  $\mu\text{m}$  ( $\nu_2$  bands) spectral regions.<sup>32</sup> As shown in Figure 1a, the  $\nu_3$  fundamental vibrational absorption band is of great importance to the atmospheric detection of  $\text{SO}_2$  in the infrared absorption spectra because of the strongest line strengths compared with the other absorption bands. However, there are some other common gas molecules in the air ( $\text{SO}_3$ ,  $\text{H}_2\text{O}$ ,  $\text{CH}_4$ , and  $\text{N}_2\text{O}$ ) having strong absorption features in the spectral range between 7.2 and 7.6  $\mu\text{m}$  spectral regions as demonstrated in Figure 1b. Particularly, the  $\text{SO}_3$  molecule shows dense and strong absorption lines between the 7.2 and 7.35  $\mu\text{m}$ . Therefore, a better excitation wavelength selection would be between 7.35 and 7.55  $\mu\text{m}$  for  $\text{SO}_2$  detection in order

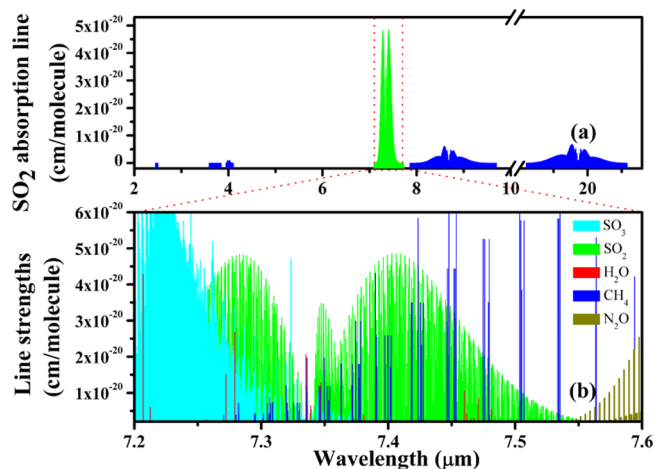


**Figure 1.** (a)  $\text{SO}_2$  absorbance spectra in the infrared region provided by the HITRAN database. (b) Absorption line parameters of  $\text{SO}_3$ ,  $\text{H}_2\text{O}$ ,  $\text{CH}_4$ ,  $\text{N}_2\text{O}$ , and  $\text{SO}_2$  molecules in the spectral range of 7.2 and 7.6  $\mu\text{m}$ .

to avoid a serious signal interference by  $\text{SO}_3$ . The more detailed  $\text{SO}_2$ ,  $\text{H}_2\text{O}$ , and  $\text{CH}_4$  molecule absorption line positions and the corresponding line strengths were shown in the Supporting Information between the wavelength of 7380 and 7430 nm. As depicted in Figure S1, the strongest absorption line of  $\text{H}_2\text{O}$  located at 7380.91 nm with the line strength of  $3.74 \times 10^{-21}$  cm/molecule, and the two strong  $\text{CH}_4$  absorption lines located at 7402.38 and 7418.17 nm with the absorption line strengths of  $2.58 \times 10^{-20}$  cm/molecule and  $3.50 \times 10^{-20}$  cm/molecule, respectively. Finally, an  $\text{SO}_2$  absorption line located at 7413.17 nm ( $1348.95 \text{ cm}^{-1}$ ) with the absorption line strength of  $4.84 \times 10^{-20}$  cm/molecule is chosen because it has the strongest line strength and is interference-free with the spectral lines of other common gases.

With the development of advanced material growth technique, the QCL source has established its presence as the most versatile semiconductor excitation source in the mid-infrared spectral region for trace gas analysis and pollution monitoring instead of a broadband light source, which usually requires an additional light path calibration system and has a poor excitation power.<sup>33–35</sup> In this manuscript, a compact and room-temperature external cavity QCL (DRS Daylight Solutions, USA, Model: 41074-MHF) was chosen as the excitation source for our sensor system, as shown in Figure 2a, which can be tuned from 7.12 to 7.65  $\mu\text{m}$  by simply rotating the diffraction grating. When the laser current and temperature were set at 700 mA and 18 °C, respectively, the laser power performance with the full tuning range is shown in Figure S2. The QCL with an external cavity design can be operated in the mode-hop-free (MHF) mode with a very narrow linewidth ( $<10$  MHz measured over  $\sim 1$  s), which provides a specified MHF tuning range of 7.2 to 7.52  $\mu\text{m}$ . The two- and three-dimensional intensity distributions of the laser beam were captured by using a pyroelectric array camera (Ophir Optronics Solutions, Ltd, Israel, model: Pyrocam-III-HR) and depicted in Figure 2b,c, which demonstrates a minimum spot size of  $<2.5$  mm ( $1/e^2$ -field radius). The nominal  $\text{TEM}_{00}$  profile has a pointing stability  $<1$  mrad at a 100 cm distance, and the maximum average output power is  $\sim 70$  mW.

Because the laser output power of the external cavity QCL was not constant at different output wavelengths,<sup>36</sup> a power meter (Ophir Optronics Solutions, Ltd, Israel, model 3A-

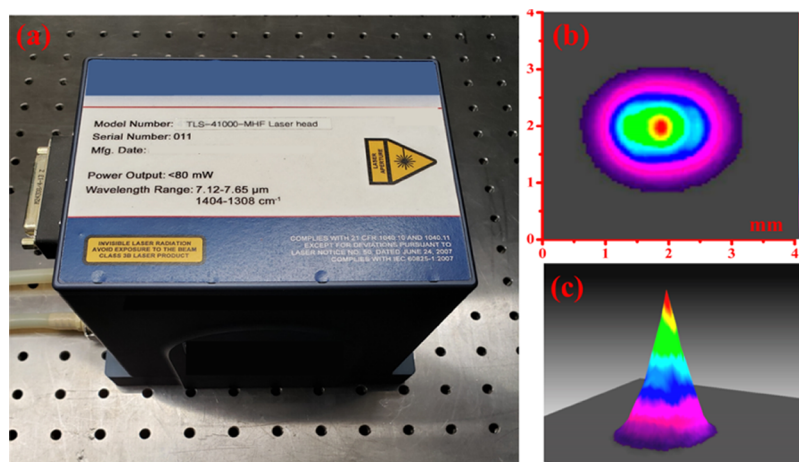


**Figure 2.** (a) QCL CW-MHF laser head. (b) Two-dimensional intensity distribution of the QCL laser beam. (c) Three-dimensional laser beam profile.

ROHS) was employed to monitor the QCL output power. Moreover, the laser head was maintained at a constant temperature of 18 °C. When the QCL current was set to 700 mA and operated in the MHF mode, the laser output power was recorded with the increase of the excitation wavelengths as depicted in Figure 3a. A relatively flat and maximum power

61.2 mW was obtained when the QCL excitation wavenumber reached 1348.95  $\text{cm}^{-1}$ . Therefore, for the following experiments, the temperature, current, and wavelength of the QCL were controlled at 18 °C, 700 mA and 7.41  $\mu\text{m}$ , respectively.

## ■ PHOTOACOUSTIC SENSOR SYSTEM

A schematic of the laser-based PAS sensor system for  $\text{SO}_2$  detection is depicted in Figure 4. In order to maintain a

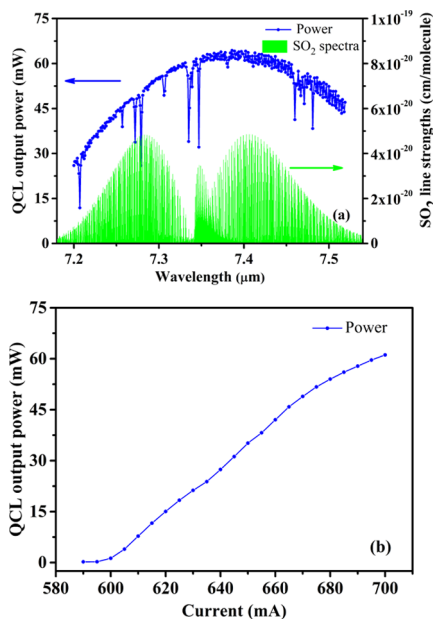


**Figure 3.** (a) QCL output power and  $\text{SO}_2$  line strengths as a function of the wavelength between 7.2 and 7.52  $\mu\text{m}$ . The laser current and temperature were set to 700 mA and 18 °C, respectively, and the laser was operated in the MHF mode. (b) QCL output power for different laser currents.

level of  $\sim 60$  mW was observed between 7.35 and 7.45  $\mu\text{m}$ , which exactly meets the requirement of the excitation wavelength mentioned above. The  $\text{SO}_2$  line strength is also depicted in Figure 3a in order to compare the relationship between the QCL power and the line strength at the same wavelength. As shown in Figure 3b, the QCL started to emit light when the input current was larger than 600 mA. Subsequently, the QCL output power increased linearly with the increase of the laser current. A maximum power point of

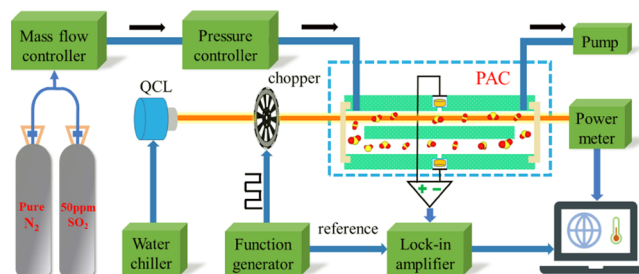


**Figure 4.** Schematic of the developed  $\text{SO}_2$  trace gas sensor system.

constant QCL temperature of 18 °C, a small closed-loop water chiller (Beijing Changliu Instruments, China, Mode: LX150) was employed. An optical chopper system (Thorlabs Inc., USA, model MC2000B) with a MC1F30 chopper blade was used to modulate the intensity of the CW QCL beam. The excitation laser power of 29.6 mW (nearly half of maximum power) was achieved after the intensity modulation. A function generator board was used to generate a square-wave modulation signal for the chopper, and the reference signal of the function generator was introduced into a lock-in amplifier (Stanford Research Systems, USA, model SR830). The filter slope and time constant of the lock-in amplifier were set to 12 dB/oct and 1 s, respectively, which corresponds to a 0.25 Hz detection bandwidth. A custom-made differential PAC with two identical resonators was designed, and the anatomical diagram of PAC is shown in Figure S3. The two parallel resonators were used for photoacoustic signal amplification, both have a 90 mm length and an 8 mm inner diameter. Two electret microphones (Primo Microphones Inc., Japan, model EM258) with the same frequency responses at  $\sim 1.5$  kHz were placed in the middle of each resonator and embedded into the walls. Moreover, two 25.4 mm  $\times$  5 mm transparent  $\text{CaF}_2$

windows and four rubber O-type rings were employed to seal the PAC as an open–open photoacoustic detector. The CaF<sub>2</sub> windows have a transmissivity of up to 91% at  $\sim 7.41 \mu\text{m}$ . The microphone current signals were directed to a custom transimpedance differential preamplifier and then transferred to the lock-in amplifier to demodulate the photoacoustic signal and retrieve the SO<sub>2</sub> concentration. The square-wave modulation frequency was equal to the fundamental longitudinal vibration frequency of the PAC. Moreover, the PAC was wrapped in an electrothermal polyimide (PI) film (Zhuhai Jiayi Electronic Technology Co., Ltd, China, model PI-100) to adjust and maintain the environment temperature between 20 and 50 °C for the following experiments. The laser power after the PAC and the SO<sub>2</sub> concentrations were recorded by a LabVIEW computer routine.

A 50 ppm SO<sub>2</sub>/N<sub>2</sub> gas mixture cylinder and a pure N<sub>2</sub> gas cylinder were used to generate different SO<sub>2</sub> concentration levels by a gas dilution system (EnviroNics Inc., USA, model EN 4000). A needle valve, a diaphragm pump (KNF Technology, Germany, model N816.3), and a pressure controller (MKS Instruments, USA, model 649B) were employed in order to control and maintain the gas flow and pressure in the sensor system. The gas flow rate of the sensor was measured by a mass flow meter (Alicat Scientific, USA, model M2SLPM). All the following experiments were carried out at atmospheric pressure.

### ■ QUALITATIVE STUDY OF ADSORPTION–DESORPTION EFFECT

During the transportation of SO<sub>2</sub>/N<sub>2</sub> gas mixtures through the PAC, an adsorption and desorption effect may appear because of the polarized molecular SO<sub>2</sub> structure. There are some similar polar molecules like ammonia and water that may have the same effect in practical concentration measurements.<sup>37</sup> The interaction processes of the target gas with the PAC walls can result in gas-phase concentration fluctuations, which affects the sensor detection sensitivity. The PAC walls serve as a “reservoir” where the gas molecules dynamically adsorb and desorb with the change of the gas molecule numbers. Equilibrium is achieved between the PAC walls and the SO<sub>2</sub> gas molecules under certain conditions.<sup>38</sup> Once the gas molecule number is higher than the equilibrium number, the reservoir will hold more SO<sub>2</sub> molecules. In general, some preventive steps are taken to eliminate effects such as polishing and heating of the cell inner-walls and increasing the gas flow rate. Assuming that the gas mixture contains the target molecules, the SO<sub>2</sub> molecule concentration  $c_1$  [cm<sup>-3</sup>] is in the gas phase, and the SO<sub>2</sub> molecule surface coverage  $c_2$  [cm<sup>-2</sup>] is in a quasi-steady state. A qualitative theoretical model was leveraged to study the adsorption–desorption processes in PAC<sup>37</sup>

$$\frac{\partial c_1}{\partial t} + \frac{\Phi}{A(x)} \frac{\partial c_1}{\partial x} + \frac{dS}{dV} \frac{\partial c_2}{\partial t} = 0 \quad (1)$$

where  $\Phi$  is the gas flow rate [cm<sup>3</sup>/s],  $A(x)$  is the PAC cross-section area [cm<sup>2</sup>],  $dS$  and  $dV$  are the cell infinitesimal surface area [cm<sup>2</sup>] and infinitesimal volume [cm<sup>3</sup>], respectively, and  $\partial c_2/\partial t$  represents the effective adsorption rate [cm<sup>-2</sup>/s]. Therefore, eq 1 indicates that the gas concentration fluctuation is because of the combined influence of the gas flow rate and the wall adsorption rate.

When a dynamic equilibrium of SO<sub>2</sub> concentration is achieved (i.e.,  $\partial c_1/\partial t$  and  $\partial c_2/\partial t$  are constant) in the reservoir, the concentration of SO<sub>2</sub> at the measurement point ( $c^m$ ) can be achieved by a partial integration from  $x = 0$  to  $x = x^m$

$$V \frac{\partial c_1^m}{\partial t} + c_1^m \Phi = c_1^{\text{in}} \Phi - \frac{\partial c_2}{\partial t} S \quad (2)$$

where  $V$  is the cell volume [cm<sup>3</sup>],  $c_1^{\text{in}}$  is the “fresh” SO<sub>2</sub> concentration [cm<sup>-3</sup>] at the entrance of the PAC ( $x = 0$ ), and  $S$  is the partial integration surface from entrance to the measurement point (cm<sup>2</sup>). The absorption-desorption effect can be negligible if:  $c_1^{\text{in}} \Phi \gg \frac{\partial c_2}{\partial t} S$ . Therefore, a higher target gas concentration  $c_1^{\text{in}}$  and a higher gas flow rate  $\Phi$  can effectively minimize the interaction processes of the target gas with the PAC walls. Moreover, the effective adsorption rate  $\partial c_2/\partial t$  and PAC surface area  $S$  should be small, which can be realized by using a PAC with a small size and a smooth inner surface. In addition, because the SO<sub>2</sub> molecules move faster at a higher environmental temperature, it makes the SO<sub>2</sub> molecules easier to move out the reservoir and hence can also reduce the absorption–desorption effect. The influences of the gas flow rate and the environmental temperature on the adsorption–desorption effect was studied experimentally in the following section.

### ■ EXPERIMENTAL RESULTS AND DISCUSSION

**Influence of the Gas Flow Rate on Adsorption–Desorption Effect.** According to the conclusions of the theoretical model, a higher gas flow rate is chosen to retard the adsorption–desorption effect. As shown in Figure 5a, a continuous flow of pure N<sub>2</sub> and 25 ppm SO<sub>2</sub>/N<sub>2</sub> gas mixture was alternately fed into the PAC at three different gas flow rates at 20 °C. First, the PAC was cleaned by pure

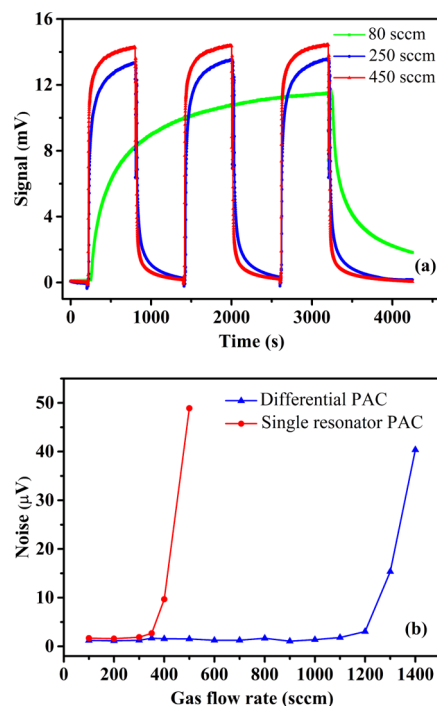


**Figure 5.** (a) Investigation of the sensor response speed at 80, 250, and 450 sccm gas flow rates. (b) Dependence of differential double-resonator and single-resonator PAC noise on different gas flow rates. The single-resonator PAC was designed with identical geometrical parameters of the differential double-resonator PAC.

$N_2$  for 1 h prior before the experiments, and then the signal was recorded for 200 s. Afterward, three 25 ppm  $SO_2/N_2$  gas mixtures were fed into the PAC at gas flow rates of 80, 250, and 450 sccm. For the gas flow rate of 80 sccm, the gas mixture lasted for 50 min and was then switched to pure  $N_2$  for 17 min. For the gas flow rates of 250 sccm and 450 sccm, the gas mixtures and pure  $N_2$  were alternately fed into the PAC and lasted for 10 min. It was observed that the time needed for stable photoacoustic signal values were different for the three different gas flow rates. A longer stabilization time was needed for a relatively slow gas flow rate. The 25 ppm  $SO_2/N_2$  gas mixture was continuously supplied into the PAC, and the photoacoustic signals for the three different gas flow rates reached almost the same values after  $\sim 2$  h. Therefore, a higher flow rate is very helpful for the detection of polar molecules by the photoacoustic trace gas sensor. Furthermore, a high gas flow rate results in a short gas-exchange time and thus improves the sensor response time.

In practice, the maximum gas flow rate was limited by the flow noise, especially for the single-resonator PAC. A perfectly symmetrical PAC can offer the possibility to significantly increase the signal-to-noise ratio (SNR) by adopting a differential circuit.<sup>39</sup> When the laser modulation frequency is consistent with the fundamental vibration frequency of the PAC, the maximum pressure oscillations are located in the middle of each resonator, whereas the minimum oscillations are located in both ends of the resonators. The pressure oscillations produced by coherent noise such as gas flow noise, external noise, and vibration are in-phase in two channels, while the pressure oscillations generated by the targeted gas molecule exist only in the resonator passed by the laser beam. As a result, the coherent noise is effectively suppressed and thus improves the SNR. As shown in Figure 5b, the gas flow noise of the developed PAC remained minimal at low flow rates but increased rapidly when the gas rate was  $>1200$  sccm. In order to compare the flow noise, a single-resonator PAC with identical geometrical parameters of the developed differential PAC was designed. The gas flow rate noise is also shown in Figure 5b. An obvious noise increase was observed when the gas flow rate  $>350$  sccm, which may result in a serious adsorption–desorption interaction of  $SO_2$  with the PAC walls. The differential structural PAC with a 3.4 times larger continuous gas flow rate indicated that the differential design can effectively reduce the gas flow noise.

**Influence of Temperature on Adsorption–Desorption Effect.** By increasing the environmental temperature of the PAC, a thermodynamic effect occurred in which the gas molecule desorption increases from the equilibrium state. For the PAS-based gas sensor, the modulation frequency of laser must be tuned to the resonance frequency. Because the PAC resonance frequency  $f$  is proportional to the ratio of the sound velocity  $v$  and the resonator length  $L$  ( $f = v/2L$ ), the resonator frequency is sensitive to temperature changes. A fixed modulation frequency of QCL laser beam results in a decreasing signal. Therefore, two PAC response curves were obtained at 20 and 50 °C and are depicted in Figure 6a. A frequency shift from  $f_1 = 1780$  Hz to  $f_2 = 1827$  Hz ( $\Delta f = 47$  Hz) was observed as a result of a change of the PAC environment temperature. Moreover, the  $Q$ -factor of the PAC remained at an almost unchanged level of 45 from 20 to 50 °C. The same results were observed when the 50 ppm  $SO_2/air$  was fed into the PAC, which indicated that the developed sensor system can also be used in air buffer gas. When the 50 ppm  $SO_2/N_2$  gas mixture was fed into the PAC, and the gas flow rate was set as 80 sccm, a higher environment temperature resulted in a faster signal increase as shown in Figure 6b. Similarly, in the opposite direction, a rapid decrease was observed when pure  $N_2$  was fed into the PAC at 50 °C.

**Sensor Performance Assessment.** Different concentrations of  $SO_2/N_2$  gas mixtures were fed into the differential PAC ranging from 0 to 20 ppm. The PAC environmental temperature was heated to 50 °C, and a gas flow rate of 600 sccm was chosen for the purpose of reducing the response time and the adsorption–desorption effect. As shown in Figure 7, the photoacoustic signal was continuously recorded when the  $SO_2$  concentrations were changed. A sensor noise level of  $1.15 \mu V$  ( $1\sigma$ ) was obtained when pure  $N_2$  was fed into the PAC. The signal fluctuations at the high concentration levels resulted from the gas dilution system because the dilution system

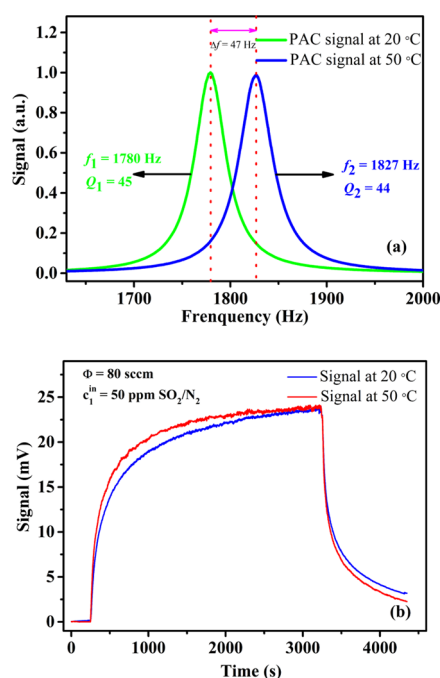


**Figure 6.** (a) Frequency response curves of the differential PAC at 20 and 50 °C. A 47 Hz resonant frequency shift was observed because of an increase of environmental temperature. (b) Continuous photoacoustic signal recorded at 20 and 50 °C, when 50 ppm  $SO_2/N_2$  gas mixture and pure  $N_2$  were alternately fed into the PAC. The gas flow rate was set at 80 sccm.

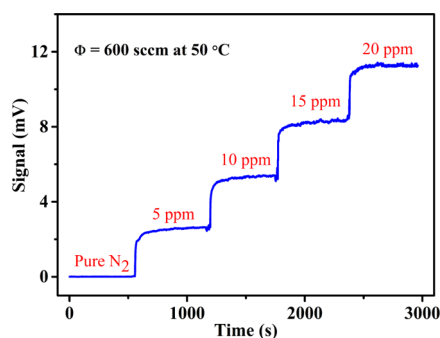


**Figure 7.** Continuous  $SO_2$  photoacoustic signals for different  $SO_2$  concentration levels ranging from 0 to 20 ppm recorded as a function of time. The differential PAC was heated to 50 °C, and the gas flow rate was set to 600 sccm.

requires some time to reach the setting value. A detection SNR of 2269 was achieved with a 5 ppm  $SO_2/N_2$  gas mixture, which resulted in a mean signal amplitude of 2.61 mV. Accordingly, a minimum detection sensitivity of 2.45 ppb was obtained with a 29.6 mW excitation power, which corresponds to a normalized noise equivalent absorption (NNEA) coefficient of  $3.32 \times 10^{-9} \text{ cm}^{-1} \text{ W/Hz}^{1/2}$  for  $SO_2$  detection at 50 °C.

In order to verify the developed  $SO_2$  sensor linearity, different  $SO_2$  concentrations were fed into the PAC ranging from 0 to 40 ppm. The  $SO_2$  signals were recorded continuously for  $>600$  s after the signal amplitudes were stable and averaged for each concentration. As plotted in Figure S4, a linear fitting  $R^2$  value of 0.999 was achieved with a slope of 0.584 mV/ppm and an intercept of 0.069 mV/ppm, which confirmed that the sensor system responds linearly to  $SO_2$  concentrations.

Subsequently, a few experiments were performed to verify that the  $SO_2$  sensor has no cross-talk problem with other gases present in the atmosphere. Because the water vapor concentration in ambient air is

0.5–4% with the variation of the geography, climate, and wet-season, a humidifier was introduced to generate different H<sub>2</sub>O concentrations in the 25 ppm SO<sub>2</sub>/N<sub>2</sub> sample. It turned out that the SO<sub>2</sub> signal remained constant in the different humidity samples.<sup>40</sup> To check CH<sub>4</sub> spectral interference, pure N<sub>2</sub> was first fed into the sensor system. Then, 25 ppm SO<sub>2</sub>/N<sub>2</sub> gas mixture was introduced into the sensor system. At last, the gas inlet of the PAC was switched to 30 ppm CH<sub>4</sub>/N<sub>2</sub> gas mixture, as shown in Figure S5. The photoacoustic signal was reduced to the  $\mu$ V level and was the same as the signal in pure N<sub>2</sub>, which indicated that there is no interference between the SO<sub>2</sub> and CH<sub>4</sub> absorption lines. The signal interference from SO<sub>3</sub> and N<sub>2</sub>O molecules can be ignored because their absorption lines are >500 nm far away from the target SO<sub>2</sub> absorption line. In order to investigate the long-term stability and precision of the developed SO<sub>2</sub> sensor system, an Allan–Werle deviation analysis was performed when pure N<sub>2</sub> was fed into the PAC. As shown in Figure S6, the SO<sub>2</sub> optimal detection limit can reach the ppt level when the integration time is >100 s.

A continuous monitoring of atmospheric SO<sub>2</sub> concentration levels was carried out to validate the sensor performance in practical application. The SO<sub>2</sub> sensor system was placed on the third floor of Shaw Amenities Building of the Shanxi University, Taiyuan, China. The gas sampling system of the PAC was connected to the outdoors of building using a Teflon tube. A 3  $\mu$ m hydrophobic poly-(tetrafluoroethylene) filter membrane was mounted at the upstream of the PAC to remove the dust and soot particles. The continuous measured SO<sub>2</sub> concentration curve (red line) with a 1 s acquisition time and the reported SO<sub>2</sub> concentration levels by the China National Environmental Monitoring Center are depicted in Figure 8. The

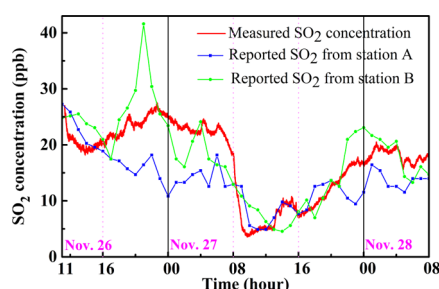


**Figure 8.** Continuous SO<sub>2</sub> concentration monitoring measured by the developed sensor system on the Shanxi University campus, Taiyuan, China and the reported SO<sub>2</sub> concentration by two nearby China National Environmental Monitoring Center.

measurement period was from November 26, 2019 to November 28, 2019. The two environmental monitoring stations A (Wucheng) and B (Xiaodian) are  $\sim$ 3 and 7 km away from our developed sensor system, where the station B is closer to the factory area. The measurements of the SO<sub>2</sub> concentration levels at the monitoring centers are based on a pulsed fluorescence method with  $\sim$ 1 min response time, while their data updating rate was one data point per hour, which implies that the data during every hour was averaged. As shown in Figure 8, the variation trend of the SO<sub>2</sub> concentrations measured by our sensor was in good agreement with that released by the station A and B. Some details of the concentration fluctuations

from the local meteorological or traffic conditions were captured by our developed sensor system because of the faster response time. However, their counterparts cannot be observed on the data curves from the monitoring centers because their data updating rate was slow.

The SO<sub>2</sub> gas sensor performance developed in this paper is compared with the previously demonstrated sensor system and shown in Table 1. An optimum SO<sub>2</sub> detection limit of 2.45 ppb is at least 1 order of magnitude better than the other reported techniques. Moreover, a fast data acquisition time of 1 s can further expand its application prospect in practice.

## CONCLUSIONS

A ppb-level PAS-based sulfur dioxide (SO<sub>2</sub>) sensor system was demonstrated by using a custom-made PAC and a mid-infrared external cavity QCL. An excitation wavelength of SO<sub>2</sub> was chosen at 7.41  $\mu$ m for the strongest line strength and without signal inferences from SO<sub>3</sub>, H<sub>2</sub>O, CH<sub>4</sub>, and N<sub>2</sub>O. By using a differential structural PAC, a high gas flow rate of up to 1200 sccm was achieved without the flow noise increasing, which is  $\sim$ 3.4 times higher than that of a single-resonator PAC. Two comparative experiments were performed in order to study the adsorption–desorption interaction processes of SO<sub>2</sub> with the PAC walls because of the polarized molecular structure of SO<sub>2</sub>. By using a higher gas flow rate and temperature, a reduced adsorption–desorption effect was achieved. When the gas flow rate was set to 600 sccm and the PAC was heated at 50  $^{\circ}$ C, a minimum detection limit of 2.45 ppb was obtained ( $\sim$ 30 times lower than the QEPAS based SO<sub>2</sub> sensor with same absorption line intensity<sup>30</sup>) for a 1 s integration time, which corresponds to a NNEA coefficient of  $3.32 \times 10^{-9} \text{ cm}^{-1} \text{ W/Hz}^{1/2}$ . Further precaution of adsorption–desorption effect can be realized by a design of a miniature polypropylene-made PAC instead of stainless steel, which can be produced by a 3D printing technique.<sup>44</sup>

## ASSOCIATED CONTENT

### Supporting Information

The Supporting Information is available free of charge at <https://pubs.acs.org/doi/10.1021/acssensors.9b02448>.

High-resolution spectra of SO<sub>2</sub>, H<sub>2</sub>O, and CH<sub>4</sub> between 7380 and 7430 nm; QCL laser power performance when operated in the full tuning range mode; anatomical diagram of the custom-made differential PAC; sensor system response linearity; sensor photoacoustic signals in pure N<sub>2</sub>, 25 ppm SO<sub>2</sub>/N<sub>2</sub>, and 30 ppm CH<sub>4</sub>/N<sub>2</sub>; and Allan–Werle deviation analysis (PDF)

## AUTHOR INFORMATION

### Corresponding Author

Lei Dong – State Key Laboratory of Quantum Optics and Quantum Optics Devices, Institute of Laser Spectroscopy and Collaborative Innovation Center of Extreme Optics, Shanxi

**Table 1.** Performance Comparison of the Developed SO<sub>2</sub> Sensor System and Previously Reported Techniques

refs	technique	light source	wavelength (nm)	power	acquisition time	sensitivity
41	absorption spectroscopy	deuterium lamp	170–230		7.5 min	12 ppb
42	PAC	diode laser	302	6.9 nW	52 s	20 ppm
13	PAC	solid-state laser	303	5 mW	1 s	74 ppb
43	iHWG	FTIR spectrometer	7168–7570		20 min	77 ppb
30	QEPAS	DFB-QCL	7240	52 mW	1 s	63 ppb
this paper	PAC	QCL	7413	29.6 mW	1 s	2.45 ppb

University, Taiyuan 030006, P. R. China; [orcid.org/0000-0001-7379-3388](https://orcid.org/0000-0001-7379-3388); Email: [donglei@sxu.edu.cn](mailto:donglei@sxu.edu.cn)

## Authors

**Xukun Yin** – State Key Laboratory of Quantum Optics and Quantum Optics Devices, Institute of Laser Spectroscopy and Collaborative Innovation Center of Extreme Optics, Shanxi University, Taiyuan 030006, P. R. China; Department of Electrical and Computer Engineering, Rice University, Houston, Texas 77005, United States; [orcid.org/0000-0003-4840-9529](https://orcid.org/0000-0003-4840-9529)

**Hongpeng Wu** – State Key Laboratory of Quantum Optics and Quantum Optics Devices, Institute of Laser Spectroscopy and Collaborative Innovation Center of Extreme Optics, Shanxi University, Taiyuan 030006, P. R. China

**Biao Li** – State Key Laboratory of Quantum Optics and Quantum Optics Devices, Institute of Laser Spectroscopy and Collaborative Innovation Center of Extreme Optics, Shanxi University, Taiyuan 030006, P. R. China

**Weiguang Ma** – State Key Laboratory of Quantum Optics and Quantum Optics Devices, Institute of Laser Spectroscopy and Collaborative Innovation Center of Extreme Optics, Shanxi University, Taiyuan 030006, P. R. China

**Lei Zhang** – State Key Laboratory of Quantum Optics and Quantum Optics Devices, Institute of Laser Spectroscopy and Collaborative Innovation Center of Extreme Optics, Shanxi University, Taiyuan 030006, P. R. China; [orcid.org/0000-0001-7247-6348](https://orcid.org/0000-0001-7247-6348)

**Wangbao Yin** – State Key Laboratory of Quantum Optics and Quantum Optics Devices, Institute of Laser Spectroscopy and Collaborative Innovation Center of Extreme Optics, Shanxi University, Taiyuan 030006, P. R. China

**Liantuan Xiao** – State Key Laboratory of Quantum Optics and Quantum Optics Devices, Institute of Laser Spectroscopy and Collaborative Innovation Center of Extreme Optics, Shanxi University, Taiyuan 030006, P. R. China; [orcid.org/0000-0003-2690-6460](https://orcid.org/0000-0003-2690-6460)

**Suotang Jia** – State Key Laboratory of Quantum Optics and Quantum Optics Devices, Institute of Laser Spectroscopy and Collaborative Innovation Center of Extreme Optics, Shanxi University, Taiyuan 030006, P. R. China

**Frank K. Tittel** – Department of Electrical and Computer Engineering, Rice University, Houston, Texas 77005, United States

Complete contact information is available at: <https://pubs.acs.org/10.1021/acssensors.9b02448>

## Author Contributions

X.Y. and H.W. contributed equally to this manuscript. X.Y., H.W., and B.L. performed the experiments. X.Y. and L.D. wrote the manuscript. L.D. provided technical guidance. W.M., L.Z., W.Y., and X.L. supported the experiments. S.J. and F.K.T. provided technical guidance and contributed to the manuscript. All the authors have given approval to the final version of the manuscript.

## Funding

L.D. acknowledges support by the National Key Research and Development Program of China (no. 2017YFA0304203); National Natural Science Foundation of China (nos. 61622503, 61575113, 11434007); and Outstanding Innovative Teams of Higher Learning Institutions of Shanxi; Shanxi “1331 Project” key subject construction. F.K.T. acknowledges support by the US National Science Foundation (NSF) ERC

MIRTHE award and the Robert Welch Foundation (Grant #C0586). X.Y. acknowledges financial support from the program of China Scholarships Council (no. 201808140194).

## Notes

The authors declare no competing financial interest.

## ABBREVIATIONS

SO<sub>2</sub>, sulfur dioxide; PAC, photoacoustic cell; PAS, photoacoustic spectroscopy; CW, continuous-wave; QCL, quantum cascade laser; ICL, interband cascade lasers; QEPAS, quartz-enhanced photoacoustic spectroscopy; NNEA, normalized noise equivalent absorption coefficient

## REFERENCES

- (1) Shaymurat, T.; Tang, Q.; Tong, Y.; Dong, L.; Liu, Y. Gas dielectric transistor of CuPc single crystalline nanowire for SO<sub>2</sub> detection down to sub-ppm levels at room temperature. *Adv. Mater.* **2013**, *25*, 2269–2273.
- (2) United States Environmental Protection Agency Website. <http://www.epa.gov> (accessed on September 29, 2019).
- (3) Huang, T.; Hou, Z.; Xu, Q.; Huang, L.; Li, C.; Zhou, Y. Polymer vesicle sensor for visual and sensitive detection of SO<sub>2</sub> in water. *Langmuir* **2017**, *33*, 340–346.
- (4) Hodgson, A. W. E.; Jacquinet, P.; Hauser, P. C. Electrochemical sensor for the detection of SO<sub>2</sub> in the low-ppb range. *Anal. Chem.* **1999**, *71*, 2831–2837.
- (5) Lee, S. C.; Hwang, B. W.; Lee, S. J.; Choi, H. Y.; Kim, S. Y.; Jung, S. Y.; Ragupathy, D.; Lee, D. D.; Kim, J. C. A novel tin oxide-based recoverable thick film SO<sub>2</sub> gas sensor promoted with magnesium and vanadium oxides. *Sens. Actuators, B* **2011**, *160*, 1328–1334.
- (6) Khan, M.; Rao, M.; Li, Q. Recent advances in electrochemical sensors for detecting toxic gases: NO<sub>2</sub>, SO<sub>2</sub> and H<sub>2</sub>S. *Sensors* **2019**, *19*, 905.
- (7) Do, J.-S.; Chen, P.-J. Amperometric sensor array for NO<sub>x</sub>, CO, O<sub>2</sub> and SO<sub>2</sub> detection. *Sens. Actuators, B* **2007**, *122*, 165–173.
- (8) Zhang, X.; Yang, B.; Wang, X.; Luo, C. Effect of plasma treatment on multi-walled carbon nanotubes for the detection of H<sub>2</sub>S and SO<sub>2</sub>. *Sensors* **2012**, *12*, 9375–9385.
- (9) Liu, Y.; Xu, X.; Chen, Y.; Zhang, Y.; Gao, X.; Xu, P.; Li, X.; Fang, J.; Wen, W. An integrated micro-chip with Ru/Al<sub>2</sub>O<sub>3</sub>/ZnO as sensing material for SO<sub>2</sub> detection. *Sens. Actuators, B* **2018**, *262*, 26–34.
- (10) Meixners, F. X.; Jaeschke, W. A. The detection of low atmospheric SO<sub>2</sub> concentrations with a chemiluminescence technique. *Int. J. Environ. Anal. Chem.* **1981**, *10*, 51–67.
- (11) Gómez, M.; Perez, E. G.; Arancibia, V.; Iribarren, C.; Bravo-Díaz, C.; García-Beltrán, O.; Aliaga, M. E. New fluorescent turn-off probes for highly sensitive and selective detection of SO<sub>2</sub> derivatives in a micellar media. *Sens. Actuators, B* **2017**, *238*, 578–587.
- (12) Hodgson, A. W. E.; Jacquinet, P.; Hauser, P. C. Electrochemical sensor for the detection of SO<sub>2</sub> in the low-ppb range. *Anal. Chem.* **1999**, *71*, 2831–2837.
- (13) Yin, X.; Dong, L.; Wu, H.; Zheng, H.; Ma, W.; Zhang, L.; Yin, W.; Xiao, L.; Jia, S.; Tittel, F. K. Highly sensitive SO<sub>2</sub> photoacoustic sensor for SF<sub>6</sub> decomposition detection using a compact mW-level diode-pumped solid-state laser emitting at 303 nm. *Opt. Express* **2017**, *25*, 32581–32590.
- (14) Niu, N.; Pu, S.; Chen, Q.; Wang, Y.; Zhao, Y.; Wu, W.; Zheng, Q. 302 nm continuous wave generation by intracavity frequency doubling of a diode-pumped Pr:YLF laser. *Appl. Opt.* **2018**, *57*, 9798–9802.
- (15) He, Y.; Ma, Y.; Tong, Y.; Yu, X.; Tittel, F. K. HCN ppt-level detection based on a QEPAS sensor with amplified laser and a miniaturized 3D-printed photoacoustic detection channel. *Opt. Express* **2018**, *26*, 9666–9675.
- (16) Liu, K.; Guo, X.; Yi, H.; Chen, W.; Zhang, W.; Gao, X. Off-beam quartz-enhanced photoacoustic spectroscopy. *Opt. Lett.* **2009**, *34*, 1594–1596.

- (17) Zheng, K.; Zheng, C.; Ma, N.; Liu, Z.; Yang, Y.; Zhang, Y.; Wang, Y.; Tittel, F. K. Near-Infrared Broadband Cavity-Enhanced Spectroscopic Multigas Sensor Using a 1650 nm Light Emitting Diode. *ACS Sens.* **2019**, *4*, 1899–1908.
- (18) Sigrist, M. W. Mid-infrared laser-spectroscopic sensing of chemical species. *J. Adv. Res.* **2015**, *6*, 529–533.
- (19) Ren, W.; Farooq, A.; Davidson, D. F.; Hanson, R. K. CO concentration and temperature sensor for combustion gases using quantum-cascade laser absorption near 4.7  $\mu\text{m}$ . *Appl. Phys. B* **2012**, *107*, 849–860.
- (20) Ren, W.; Jiang, W.; Tittel, F. K. Single-QCL-based absorption sensor for simultaneous trace-gas detection of  $\text{CH}_4$  and  $\text{N}_2\text{O}$ . *Appl. Phys. B* **2014**, *117*, 245–251.
- (21) Cao, Y.; Sanchez, N. P.; Jiang, W.; Griffin, R. J.; Xie, F.; Hughes, L. C.; Zah, C.-e.; Tittel, F. K. Simultaneous atmospheric nitrous oxide, methane and water vapor detection with a single continuous wave quantum cascade laser. *Opt. Express* **2015**, *23*, 2121–2132.
- (22) Hayden, J.; Baumgartner, B.; Waclawek, J. P.; Lendl, B. Mid-infrared sensing of CO at saturated absorption conditions using intracavity quartz-enhanced photoacoustic spectroscopy. *Appl. Phys. B* **2019**, *125*, 159.
- (23) Spagnolo, V.; Patimisco, P.; Borri, S.; Scamarcio, G.; Bernacki, B. E.; Kriesel, J. Part-per-trillion level  $\text{SF}_6$  detection using a quartz enhanced photoacoustic spectroscopy-based sensor with single-mode fiber-coupled quantum cascade laser excitation. *Opt. Lett.* **2012**, *37*, 4461–4463.
- (24) Patimisco, P.; Sampaolo, A.; Zheng, H.; Dong, L.; Tittel, F. K.; Spagnolo, V. Quartz-enhanced photoacoustic spectrophones exploiting custom tuning forks: a review. *Adv. Phys.: X* **2017**, *2*, 169–187.
- (25) Patimisco, P.; Sampaolo, A.; Dong, L.; Tittel, F. K.; Spagnolo, V. Recent advances in quartz enhanced photoacoustic sensing. *Appl. Phys. Rev.* **2018**, *5*, 011106.
- (26) Sampaolo, A.; Patimisco, P.; Giglio, M.; Vitiello, M.; Beere, H.; Ritchie, D.; Scamarcio, G.; Tittel, F.; Spagnolo, V. Improved tuning fork for terahertz quartz-enhanced photoacoustic spectroscopy. *Sensors* **2016**, *16*, 439.
- (27) Somesfalean, G.; Zhang, Z. G.; Sjöholm, M.; Svanberg, S. All-diode-laser ultraviolet absorption spectroscopy for sulfur dioxide detection. *Appl. Phys. B* **2005**, *80*, 1021–1025.
- (28) Zhang, Y.; Wang, Y.; Liu, Y.; Dong, X.; Xia, H.; Zhang, Z.; Li, J. Optical  $\text{H}_2\text{S}$  and  $\text{SO}_2$  sensor based on chemical conversion and partition differential optical absorption spectroscopy. *Spectrochim. Acta, Part A* **2019**, *210*, 120–125.
- (29) Yin, X.; Dong, L.; Wu, H.; Zhang, L.; Ma, W.; Yin, W.; Xiao, L.; Jia, S.; Tittel, F. K. Highly sensitive photoacoustic multicomponent gas sensor for  $\text{SF}_6$  decomposition online monitoring. *Opt. Express* **2019**, *27*, A224–A234.
- (30) Waclawek, J. P.; Lewicki, R.; Moser, H.; Brandstetter, M.; Tittel, F. K.; Lendl, B. Quartz-enhanced photoacoustic spectroscopy-based sensor system for sulfur dioxide detection using a CW DFB-QCL. *Appl. Phys. B* **2014**, *117*, 113–120.
- (31) Kosterev, A. A.; Tittel, F. K.; Serebryakov, D. V.; Malinovsky, A. L.; Morozov, I. V. Applications of quartz tuning forks in spectroscopic gas sensing. *Rev. Sci. Instrum.* **2005**, *76*, 043105.
- (32) Rothman, L. S.; Gordon, I. E.; Babikov, Y.; Barbe, A.; Chris Benner, D.; Bernath, P. F.; Birk, M.; Bizzocchi, L.; Boudon, V.; Brown, L. R.; Campargue, A.; Chance, K.; Cohen, E. A.; Coudert, L. H.; Devi, V. M.; Drouin, B. J.; Fayt, A.; Flaud, J.-M.; Gamache, R. R.; Harrison, J. J.; Hartmann, J.-M.; Hill, C.; Hodges, J. T.; Jacquemart, D.; Jolly, A.; Lamouroux, J.; Le Roy, R. J.; Li, G.; Long, D. A.; Lyulin, O. M.; Mackie, C. J.; Massie, S. T.; Mikhailenko, S.; Müller, H. S. P.; Naumenko, O. V.; Nikitin, A. V.; Orphal, J.; Perevalov, V.; Perrin, A.; Polovtseva, E. R.; Richard, C.; Smith, M. A. H.; Starikova, E.; Sung, K.; Tashkun, S.; Tennyson, J.; Toon, G. C.; Tyuterev, V. G.; Wagner, G. The HITRAN2012 molecular spectroscopic database. *J. Quant. Spectrosc. Radiat. Transfer* **2013**, *130*, 4–50.
- (33) Yi, H.; Maamary, R.; Gao, X.; Sigrist, M. W.; Fertein, E.; Chen, W. Short-lived species detection of nitrous acid by external-cavity quantum cascade laser based quartz-enhanced photoacoustic absorption spectroscopy. *Appl. Phys. Lett.* **2015**, *106*, 101109.
- (34) Maulini, R.; Mohan, A.; Giovannini, M.; Faist, J.; Gini, E. External cavity quantum-cascade laser tunable from 8.2 to 10.4  $\mu\text{m}$  using a gain element with a heterogeneous cascade. *Appl. Phys. Lett.* **2006**, *88*, 201113.
- (35) Spagnolo, V.; Patimisco, P.; Borri, S.; Scamarcio, G.; Bernacki, B. E.; Kriesel, J. Mid-infrared fiber-coupled QCL-QEPAS sensor. *Appl. Phys. B* **2013**, *112*, 25–33.
- (36) Hugi, A.; Maulini, R.; Faist, J. External cavity quantum cascade laser. *Semicond. Sci. Technol.* **2010**, *25*, 083001.
- (37) Schmohl, A.; Miklos, A.; Hess, P. Effects of adsorption-desorption processes on the response time and accuracy of photoacoustic detection of ammonia. *Appl. Opt.* **2001**, *40*, 2571–2578.
- (38) Miklós, A.; Hessa, P.; Bozóki, Z. Application of acoustic resonators in photoacoustic trace gas analysis and metrology. *Rev. Sci. Instrum.* **2001**, *72*, 1937–1955.
- (39) Lee, C.-M.; Bychkov, K. V.; Kapitanov, V. A.; Karapuzikov, A. I.; Ponomarev, Y. N.; Sherstov, I. V.; Vasiliev, V. A. High-sensitivity laser photoacoustic leak detector. *Opt. Eng.* **2007**, *46*, 064302.
- (40) Yin, X.; Dong, L.; Wu, H.; Zheng, H.; Ma, W.; Zhang, L.; Yin, W.; Jia, S.; Tittel, F. K. Sub-ppb nitrogen dioxide detection with a large linear dynamic range by use of a differential photoacoustic cell and a 3.5 W blue multimode diode laser. *Sens. Actuators, B* **2017**, *247*, 329–335.
- (41) Zhang, Y.; Wang, Y.; Liu, Y.; Dong, X.; Xia, H.; Zhang, Z.; Li, J. Optical  $\text{H}_2\text{S}$  and  $\text{SO}_2$  sensor based on chemical conversion and partition differential optical absorption spectroscopy. *Spectrochim. Acta, Part A* **2019**, *210*, 120–125.
- (42) Somesfalean, G.; Zhang, Z. G.; Sjöholm, M.; Svanberg, S. All-diode-laser ultraviolet absorption spectroscopy for sulfur dioxide detection. *Appl. Phys. B* **2005**, *80*, 1021–1025.
- (43) Petrucu, J. F. d. S.; Wilk, A.; Cardoso, A. A.; Mizaikoff, B. Online Analysis of  $\text{H}_2\text{S}$  and  $\text{SO}_2$  via Advanced Mid-Infrared Gas Sensors. *Anal. Chem.* **2015**, *87*, 9605–9611.
- (44) Bauer, R.; Stewart, G.; Johnstone, W.; Boyd, E.; Lengden, M. 3D-printed miniature gas cell for photoacoustic spectroscopy of trace gases. *Opt. Lett.* **2014**, *39*, 4796–4799.